Geophys. J. Int. (2002) **148,** 506–519

Three-dimensional inversion of multitransmitter electromagnetic data based on the localized quasi-linear approximation

M. S. Zhdanov and E. Tartaras

Department of Geology and Geophysics, University of Utah, Salt Lake City UT 84112*, USA. E-mail: mzhdanov@mines.utah.edu*

Accepted 2001 August 22. Received 2001 August 22; in original form 2000 September 28

SUMMARY

Three-dimensional (3-D) electromagnetic (EM) inversion is increasingly important for the correct interpretation of EM data sets in complex environments. To this end, several approximate solutions have been developed that allow the construction of relatively fast inversion schemes. We have developed a localized quasi-linear (LQL) approximation that is source-independent and, therefore, appropriate for multisource array-type surveys, typical in many geophysical applications, such as airborne EM, cross-well tomography, and well logging. This method is based on the assumption that the anomalous electric field within an inhomogeneous domain is linearly proportional to the background electric field through an electrical reflectivity tensor $\hat{\boldsymbol{\lambda}}$. This tensor is determined by solving a source-independent minimization problem based on the integral equation for the scattering currents. We have also developed a new, fast 3-D EM inversion method, based on this new approximation, and applied it to synthetic and real helicopter-borne EM data. The results demonstrate the stability and efficiency of the method and show that the LQL approximation can be a practical solution to the problem of 3-D inversion of multitransmitter frequency-domain EM data.

Key words: electrical conductivity, electromagnetic induction, electromagnetic methods, electromagnetic modelling, electromagnetic surveys, inversion.

1 INTRODUCTION

Electromagnetic (EM) exploration of the Earth's interior has advanced in recent years through the development of new techniques for modelling and inverting EM field data. The integral equation (IE) method is a powerful tool for EM numerical modelling (Weidelt 1975; Hohmann 1975; Dmitriev & Pozdnyakova 1992). This method is based on expressing the electromagnetic fields as a system of integral equations with respect to the anomalous currents within an inhomogeneity. One can transform the integral equations into a system of linear algebraic equations by approximating the anomalous current distribution, $\mathbf{j}^a$, by piecewise constant functions. The algebraic system is then solved numerically (Xiong 1992), and the EM field is calculated at the receivers. The main difficulty with this technique is the size of the matrix of the linear system of equations, which can demand excessive computer memory and calculation time. This limitation of the integral equation technique becomes critical in inverse problems that require multiple forward modelling calculations for many different geoelectrical models.

A novel approach to 3-D EM modelling based on linearization of the integral equations for scattered EM fields has been developed recently (Zhdanov & Fang 1996a, 1997). Within this method, called the quasi-linear (QL) approximation, the anomalous currents are assumed to be proportional to the background (normal) field, $\mathbf{E}^b$, through an electrical reflectivity tensor, $\hat{\boldsymbol{\lambda}}$. This tensor is determined by solving a minimization problem based on an integral equation for the scattering currents. The electrical reflectivity tensor has been shown (Zhdanov & Fang 1996a) to be slowly varying, and therefore this minimization problem can be computed on a much coarser grid than the field itself, thereby significantly speeding up the calculations. Hence, this problem is much less time consuming than the full IE method, while still providing satisfactory accuracy. Moreover, the introduction of the electrical reflectivity tensor allows the transformation of the original non-linear inverse problem, with respect to the anomalous conductivity, to a series of linear inverse problems (Zhdanov & Fang 1996b). Thus, the QL approximation can be a very useful tool for 3-D EM inversion (Zhdanov & Fang 1999).

One problem, however, with the QL approximation is the fact that the electrical reflectivity tensor depends on the illuminating (background) field. In other words, for each new position of the transmitter we have to recalculate the tensor coefficient $\hat{\boldsymbol{\lambda}}$. This slows down the calculations for multitransmitter arrays, which are used in many geophysical applications, such as airborne EM, cross-well tomography and well logging. Thus, 3-D inversion of such data becomes impractical. We have, therefore, developed a new approach to the QL approximation

based on the localized electrical reflectivity tensor, which is independent of the source position. This new approach is called the localized quasi-linear (LQL) approximation, and combines the ideas of the localized non-linear (LN) approximation suggested by Habashy *et al.* (1993) and the original QL approximation. It extends to 3-D scenarios the principles of the modified QL approximation that were applied by Zhou & Liu (2000) to 2-D radar-diffraction tomography. Here we use the LQL approximation for 3-D inversion of EM data in the quasi-static domain.

2 BACKGROUND OF THE QUASI-LINEAR APPROXIMATION

For completeness, we begin our paper with the formulation of the basic principles of the QL approximation. We consider a 3-D geoelectric model with a background complex conductivity $\tilde{\sigma}_b$ and a local inhomogeneity D with arbitrary spatial variations of complex conductivity $\tilde{\sigma}=\tilde{\sigma}_b+\Delta\tilde{\sigma}$. Complex conductivity includes the effect of displacement currents: $\tilde{\sigma}=\sigma-i\omega\varepsilon$, where σ and ε are the electrical conductivity and the dielectric permittivity, respectively. We assume that $\mu=\mu_0=4\pi\times10^{-7}$ H m^{-1}, where μ_0 is the free-space magnetic permeability. The model is excited by an electromagnetic field that is generated by an arbitrary source. This field is time harmonic as $e^{-i\omega t}$. The electromagnetic fields in this model can be presented as the sum of background and anomalous fields:

$$\mathbf{E}=\mathbf{E}^b+\mathbf{E}^a\,,\quad \mathbf{H}=\mathbf{H}^b+\mathbf{H}^a\,, \tag{1}$$

where the background field is a field generated by the given sources in the model with the background distribution of conductivity $\tilde{\sigma}_b$, and the anomalous field is produced by the anomalous conductivity distribution $\Delta\tilde{\sigma}$.

It is well known that the anomalous field can be presented as an integral over the anomalous currents in the inhomogeneous domain D (Hohmann 1975; Weidelt 1975):

$$\mathbf{E}^a(\mathbf{r}_j)=\iiint_D \widehat{\mathbf{G}}_E(\mathbf{r}_j|\mathbf{r})\mathbf{j}^a(\mathbf{r})dv=\mathbf{G}_\mathbf{E}(\mathbf{j}^a)\,, \tag{2}$$

$$\mathbf{H}^a(\mathbf{r}_j)=\iiint_D \widehat{\mathbf{G}}_H(\mathbf{r}_j|\mathbf{r})\mathbf{j}^a(\mathbf{r})dv=\mathbf{G}_\mathbf{H}(\mathbf{j}^a)\,, \tag{3}$$

where $\widehat{\mathbf{G}}_E(\mathbf{r}_j|\mathbf{r})$ and $\widehat{\mathbf{G}}_H(\mathbf{r}_j|\mathbf{r})$ are the electric and magnetic Green's tensors defined for an unbounded conductive medium with the background conductivity $\tilde{\sigma}_b$; $\mathbf{G}_\mathbf{E}$ and $\mathbf{G}_\mathbf{H}$ are the corresponding Green's linear operators, and anomalous current $\mathbf{j}^a$ is determined by the equation

$$\mathbf{j}^a=\Delta\tilde{\sigma}\mathbf{E}=\Delta\tilde{\sigma}\left(\mathbf{E}^b+\mathbf{E}^a\right). \tag{4}$$

Using Green's operators, one can calculate the electromagnetic field at any point $\mathbf{r}_j$, if the electric field is known within the inhomogeneity:

$$\mathbf{E}(\mathbf{r}_j)=\mathbf{G}_\mathbf{E}(\Delta\tilde{\sigma}\mathbf{E})+\mathbf{E}^b(\mathbf{r}_j)\,, \tag{5}$$

$$\mathbf{H}(\mathbf{r}_j)=\mathbf{G}_\mathbf{H}(\Delta\tilde{\sigma}\mathbf{E})+\mathbf{H}^b(\mathbf{r}_j)\,. \tag{6}$$

Eq. (5) becomes the integral equation with respect to the electric field $\mathbf{E}(\mathbf{r})$, if $\mathbf{r}_j\in D$.

The quasi-linear approximation is based on the assumption that the anomalous field $\mathbf{E}^a$ inside the inhomogeneous domain is linearly proportional to the background field $\mathbf{E}^b$ through some tensor $\hat{\lambda}$ (Zhdanov & Fang 1996a):

$$\mathbf{E}^a(\mathbf{r})\approx\hat{\lambda}(\mathbf{r})\mathbf{E}^b(\mathbf{r})\,. \tag{7}$$

Substituting eq. (7) into eq. (4) and that result into eq. (5), we obtain the QL approximation $\mathbf{E}^a_{QL}(\mathbf{r})$ for the anomalous field:

$$\mathbf{E}^a_{QL}(\mathbf{r})=\mathbf{G}_\mathbf{E}\left(\Delta\tilde{\sigma}\left[\hat{I}+\hat{\lambda}(\mathbf{r})\right]\mathbf{E}^b\right), \tag{8}$$

where $\hat{I}$ is the identity tensor.

The electrical reflectivity tensor is found by solving the minimization problem over the corresponding domain D of the anomalous conductivity distribution:

$$\left\|\hat{\lambda}(\mathbf{r}_j)\mathbf{E}^b(\mathbf{r}_j)-\mathbf{G}_\mathbf{E}\left(\Delta\tilde{\sigma}\left(\hat{I}+\hat{\lambda}(\mathbf{r})\right)\mathbf{E}^b\right)\right\|_{L_2(D)}=\min\,. \tag{9}$$

3 LOCALIZED QUASI-LINEAR APPROXIMATION

Let us analyse again eqs (7) and (8) of the QL approximation. Following Habashy *et al.* (1993) and Torres-Verdin & Habashy (1994), we can take into account that the Green's tensor $\widehat{G}_E(\mathbf{r}_j|\mathbf{r})$ exhibits either a singularity or a peak at the point where $\mathbf{r}_j=\mathbf{r}$. Therefore, one can expect that the dominant contribution to the integral $\mathbf{G}_\mathbf{E}(\Delta\tilde{\sigma}\lambda\mathbf{E}^b)$ in eq. (8) is from some vicinity of the point $\mathbf{r}_j=\mathbf{r}$. Assuming also that $\mathbf{E}^b(\mathbf{r}_j)$ is slowly varying within the domain D, one can rewrite eq. (8) as

$$\mathbf{E}^a_{QL}(\mathbf{r}_j)\approx\mathbf{G}_\mathbf{E}\left(\Delta\tilde{\sigma}\left[\hat{I}+\hat{\lambda}(\mathbf{r})\right]\right)\mathbf{E}^b(\mathbf{r}_j)\,, \tag{10}$$

where

$$\mathbf{G}_\mathbf{E}\left(\Delta\tilde{\sigma}\left[\hat{I}+\hat{\lambda}(\mathbf{r})\right]\right)=\int_D \widehat{\mathbf{G}}_E(\mathbf{r}_j|\mathbf{r})\Delta\tilde{\sigma}(\mathbf{r})\left[\hat{I}+\hat{\lambda}(\mathbf{r})\right]dv\,. \tag{11}$$

Comparing eqs (7) and (10), we find that inside the domain D,

$$\mathbf{E}^a_{QL}(\mathbf{r}_j)=\hat{\lambda}(\mathbf{r}_j)\mathbf{E}^b(\mathbf{r}_j)\approx\mathbf{G}_\mathbf{E}\left(\Delta\tilde{\sigma}\left[\hat{I}+\hat{\lambda}(\mathbf{r})\right]\right)\mathbf{E}^b(\mathbf{r}_j)\,, \tag{12}$$

where $\mathbf{r}_j\in D$, and the electrical reflectivity tensor can be determined from the solution of a minimization problem similar to eq. (9):

$$\left\|\hat{\lambda}(\mathbf{r}_j)\mathbf{E}^b(\mathbf{r}_j)-\mathbf{G}_\mathbf{E}\left(\Delta\tilde{\sigma}\left[\hat{I}+\hat{\lambda}(\mathbf{r})\right]\right)\mathbf{E}^b(\mathbf{r}_j)\right\|_{L_2(D)}=\min\,. \tag{13}$$

Taking into account that

$$\begin{aligned}&\left\|\hat{\lambda}(\mathbf{r}_j)\mathbf{E}^b(\mathbf{r}_j)-\mathbf{G}_\mathbf{E}\left(\Delta\tilde{\sigma}\left[\hat{I}+\hat{\lambda}(\mathbf{r})\right]\right)\mathbf{E}^b(\mathbf{r}_j)\right\|_{L_2(D)}\\&\quad\le\left\|\hat{\lambda}(\mathbf{r}_j)-\mathbf{G}_\mathbf{E}\left(\Delta\tilde{\sigma}\left[\hat{I}+\hat{\lambda}(\mathbf{r})\right]\right)\right\|_{L_2(D)}\left\|\mathbf{E}^b\mathbf{r}_j)\right\|_{L_2(D)}\,,\end{aligned} \tag{14}$$

we can replace the minimization problem (13) with the analogous problem

$$\left\|\hat{\lambda}(\mathbf{r}_j)-\mathbf{G}_\mathbf{E}\left(\Delta\tilde{\sigma}\left[\hat{I}+\hat{\lambda}(\mathbf{r})\right]\right)\right\|_{L_2(D)}=\min\,. \tag{15}$$

The solution of eq. (15) gives us *a localized electrical reflectivity tensor* $\hat{\lambda}_L(\mathbf{r})$, which is obviously source-independent. We will call eq. (8), with $\hat{\lambda}_L(\mathbf{r})$ determined according to eq. (15), *a localized quasi-linear (LQL) approximation:*

$$\mathbf{E}^a_{LQL}(\mathbf{r}_j)=\mathbf{G}_\mathbf{E}\left(\Delta\tilde{\sigma}\left[\hat{I}+\hat{\lambda}_L(\mathbf{r})\right]\mathbf{E}^b(\mathbf{r})\right). \tag{16}$$

In a similar way we can find a localized quasi-linear approximation for the magnetic field:

$$\mathbf{H}^a_{LQL}(\mathbf{r}_j)=\mathbf{G}_\mathbf{H}\left(\Delta\tilde{\sigma}\left[\hat{I}+\hat{\lambda}_L(\mathbf{r})\right]\mathbf{E}^b(\mathbf{r})\right). \tag{17}$$

The LQL approximation has a similar background to the localized non-linear (LN) approximation (Habashy *et al.* 1993; Torres-Verdin & Habashy 1994), but there are some important differences. The LN approximation also replaces the total field inside the inhomogeneity with a product of the background field and the depolarization tensor $\widehat{\mathbf{\Gamma}}(\mathbf{r})$:

$$\mathbf{E}_{\mathrm{LN}}(\mathbf{r}) \approx \widehat{\mathbf{\Gamma}}(\mathbf{r})\mathbf{E}^{\mathrm{b}}(\mathbf{r}) . \tag{18}$$

However, the depolarization tensor is defined explicitly through an integral of the anomalous conductivity. In contrast, for the LQL approximation the electrical reflectivity tensor is determined as the solution of the minimization problem, eq. (15). Note also that the electrical reflectivity tensor has been shown to be slowly varying in the spatial domain (Zhdanov & Fang 1996a), and therefore it is possible to speed up the calculation (15) by using a much coarser grid than that used for the EM field itself. However, this is not necessary, and we do not employ a coarser grid in this work.

Another important difference between the LQL approximation and the LN approximation is that in our method we can choose different types of reflectivity tensor. For example, we can introduce scalar or diagonal reflectivity tensors.

In the case of a scalar reflectivity tensor, $\hat{\boldsymbol{\lambda}}_{\mathrm{L}} = \lambda_{\mathrm{L}}\hat{\boldsymbol{I}}$ (Zhdanov & Fang 1996a),

$$\mathbf{E}^{\mathrm{a}}(\mathbf{r}) \approx \lambda_{\mathrm{L}}(\mathbf{r})\mathbf{E}^{\mathrm{b}}(\mathbf{r}) . \tag{19}$$

Substituting eq. (19) into eq. (16), we obtain a scalar LQL approximation $\mathbf{E}^{\mathrm{a}}_{\mathrm{LQL}}(\mathbf{r})$ for the anomalous field:

$$\mathbf{E}^{\mathrm{a}}_{\mathrm{LQL}}(\mathbf{r}_j) = \mathbf{G}_{\mathbf{E}}\left(\Delta\tilde{\sigma}(1+\lambda_{\mathrm{L}}(\mathbf{r}))\mathbf{E}^{\mathrm{b}}\right) , \tag{20}$$

where the scalar reflectivity coefficient $\lambda_{\mathrm{L}}(\mathbf{r})$ is determined by the solution of the optimization problem

$$\left\|\lambda_{\mathrm{L}}(\mathbf{r}_j)\hat{\boldsymbol{I}} - \mathbf{G}_{\mathbf{E}}(\Delta\tilde{\sigma}(1+\lambda_{\mathrm{L}}(\mathbf{r})))\right\|_{L_2(D)} = \min . \tag{21}$$

In the special case of a diagonal reflectivity tensor

$$\hat{\boldsymbol{\lambda}}_{\mathrm{L}} = \operatorname{diag}\boldsymbol{\lambda}_{\mathrm{L}} = \begin{bmatrix} \lambda_x & 0 & 0 \\ 0 & \lambda_y & 0 \\ 0 & 0 & \lambda_z \end{bmatrix} , \tag{22}$$

where $\boldsymbol{\lambda}_{\mathrm{L}}$ is a reflectivity vector,

$$\boldsymbol{\lambda}_{\mathrm{L}} = \begin{bmatrix} \lambda_x \\ \lambda_y \\ \lambda_z \end{bmatrix} , \tag{23}$$

we thus have

$$\mathbf{E}^{\mathrm{a}}(\mathbf{r}) \approx \operatorname{diag}\boldsymbol{\lambda}_{\mathrm{L}}(\mathbf{r})\mathbf{E}^{\mathrm{b}}(\mathbf{r}) . \tag{24}$$

Substituting eq. (24) into eq. (16), we obtain a diagonal LQL approximation $\mathbf{E}^{\mathrm{a}}_{\mathrm{LQL}}(\mathbf{r})$ for the anomalous field:

$$\mathbf{E}^{\mathrm{a}}_{\mathrm{LQL}}(\mathbf{r}_j) = \mathbf{G}_{\mathbf{E}}\left(\Delta\tilde{\sigma}\left(\hat{\boldsymbol{I}} + \operatorname{diag}\boldsymbol{\lambda}_{\mathrm{L}}(\mathbf{r})\right)\mathbf{E}^{\mathrm{b}}\right) , \tag{25}$$

where the reflectivity vector $\boldsymbol{\lambda}_{\mathrm{L}}(\mathbf{r})$ is determined by the solution of an optimization problem

$$\left\|\operatorname{diag}\boldsymbol{\lambda}_{\mathrm{L}}(\mathbf{r}_j) - \mathbf{G}_{\mathbf{E}}\left(\Delta\tilde{\sigma}\left(\hat{\boldsymbol{I}} + \operatorname{diag}\boldsymbol{\lambda}_{\mathrm{L}}(\mathbf{r})\right)\right)\right\|_{L_2(D)} = \min . \tag{26}$$

3.1 Selection of the different types of electrical reflectivity tensor

The choice of electrical reflectivity tensor is related to the physics of the problem, and the accuracy and speed required in the computations.

The assumption of a scalar reflectivity tensor implies that the anomalous electric field, $\mathbf{E}^{\mathrm{a}}$, inside the anomaly is parallel to the background field, $\mathbf{E}^{\mathrm{b}}$. This is because all three components of the anomalous field are related to the corresponding component of the background field through the same coefficient of proportionality, λ. This assumption can be valid in some special cases, such as when a thin horizontal plate-like conductor is excited by the EM field of a horizontal loop at the surface. However, it is clearly not always valid. A more accurate computation of the anomalous EM field is achieved using the diagonal reflectivity tensor. In this case each component of the anomalous field is only related to the corresponding component of the background field, but now the coefficients of proportionality can be different. Thus the total anomalous field is not necessarily parallel to the background field. Finally, there are cases when a full reflectivity tensor is required in order to accurately describe the induction process. An example would be the anomalous EM fields induced in a thin vertical plate-like conductor excited by the field of a horizontal loop at the surface.

In fully 3-D cases, the physical considerations listed above show that more complex reflectivity tensors will give a more accurate approximation. As long as only forward modelling is considered, the differences in calculation times are negligible. However, since our goal is to use the LQL approximation in a 3-D inversion scheme, further analysis is required. This analysis follows in the inversion section.

3.2 Numerical examples of the LQL approximation

In this section we compare the anomalous magnetic field computed using the LQL approximation with the values obtained from the full IE method, and other approximations (Born, QL). The IE responses are calculated using the SYSEM program (Xiong 1992).

First, we analyse the results of a numerical calculation for Model 1, presented in Fig. 1. It consists of a homogeneous half-space with a resistivity of 100 Ω m and a conductive rectangular inclusion with a resistivity of 1 Ω m. The model is excited by a 10 m × 10 m rectangular transmitter loop, which carries a current of 1 A and is 50 m to the left of the model. This specific model is taken from the paper by Zhdanov & Fang (1996a), where they compared the responses of full IE, the Born approximation, the QL approximation with a diagonal reflectivity tensor and the QL approximation with a scalar reflectivity tensor. Here, we reproduce their results for full IE, the Born approximation and the scalar QL approximation, and compare them with the results for the scalar LQL approximation. The responses are computed for receivers located along the *Y*-axis on the surface and at a frequency of 100 Hz. Fig. 2 shows the comparison for the real and imaginary parts of the anomalous magnetic field. One can see that the QL and LQL approximations produce results close to the full IE solution, while the Born approximation produces a curve that has the correct shape but an incorrect magnitude. There are small amplitude differences observed between the full IE solution and

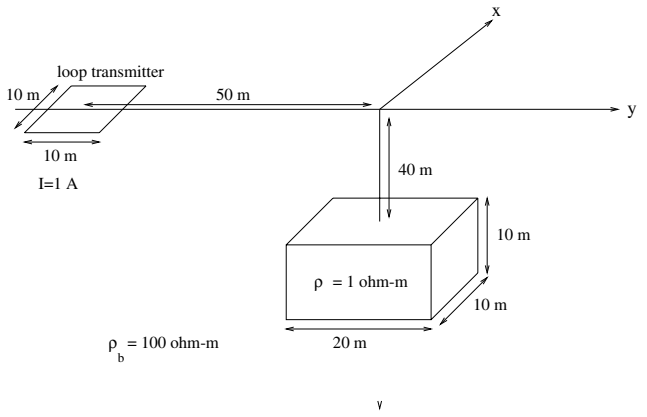

Figure 1. Model 1: 3-D geoelectric model of a conductive anomaly in a homogeneous half-space with rectangular loop excitation.

the QL and LQL approximations, and negligible differences between the two approximations. The differences between the two approximate solutions and the full IE solution (observed mainly in the real part of the response near the centre of the profile) arise from the fact that the normal field in the model is asymmetrical. This results in the same type of asymmetry in the IE solution, but is not properly accounted for in the approximate solutions (they both use a scalar reflectivity tensor and assume the anomalous field to be parallel to the background field). The differences between the QL and LQL approximations are caused by the fact that the value of the normal electric field inside the anomalous domain is not included in the minimization problem solved in the LQL scheme.

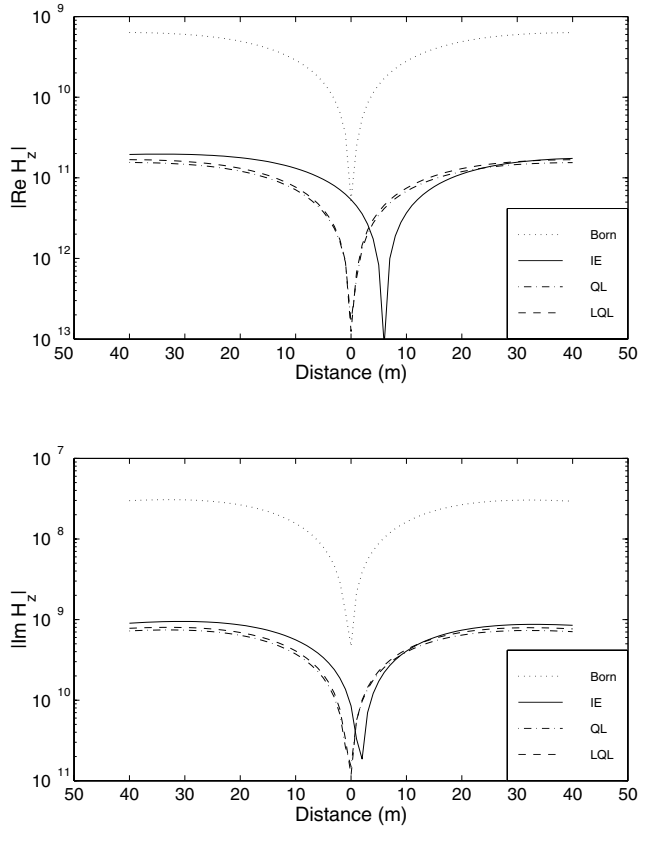

Figure 2. Numerical comparison of the full IE solution, Born approximation, scalar QL approximation, and scalar LQL approximation at frequency $f = 100$ Hz for Model 1 (Fig. 1). Absolute values of the real and imaginary parts of the anomalous magnetic field are presented at receivers on the surface along the *Y*-axis.

The second model we have used in these tests is more similar to a model where the LQL approximation is likely to be used. Model 2 is shown in Fig. 3. It consists of a homogeneous half-space with a resistivity of 500 Ω m and a conductive rectangular inclusion with a resistivity of 20 Ω m. A helicopter-borne EM survey is simulated on a profile along the *Y*-axis passing above the centre of the body at a height of 30 m above the ground. A vertical coplanar coil pair with 8 m horizontal separation is used to measure the H_{zz} response at 56 kHz. The responses, calculated using the full IE method and the Born, QL and LQL approximations are shown in Fig. 4. The Born approximation yields a response that is very different from the full IE solution, whereas all the other responses are close in amplitude. Fig. 5 shows the same results, but in this case we have omitted the Born approximation results, so that we can compare the other responses more accurately. We also added the responses of the diagonal and tensor LQL approximations. The scalar LQL approximation agrees well with the full IE solution, and only at the points of the profile where the response from the anomaly displays a maximum does it become slightly worse than the scalar QL approximation. This is a direct consequence of localizing the QL approximation. The reason is that, at these points of the profile, the normal field inside the anomaly shows (relatively) significant variations. In particular, it is much larger on the side of the body facing the transmitter than on the opposite side. Thus, the assumption made in the LQL theory concerning the normal field in the anomaly does not represent reality quite as accurately. On the other hand, the more accurate tensor forms of the LQL approximation are increasingly closer to the full IE solution.

4 3-D INVERSION SCHEME BASED ON THE LQL APPROXIMATION

In this section we describe the 3-D inversion scheme we have developed, based on the LQL approximation.

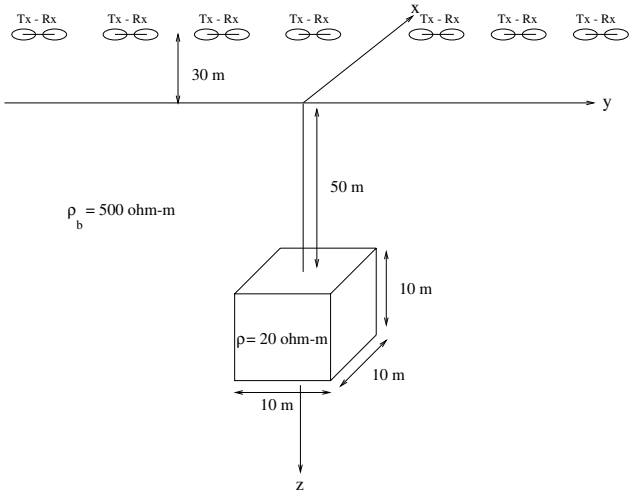

Figure 3. Model 2: 3-D geoelectric model of a conductive anomaly in a homogeneous half-space with a simulated helicopter-borne survey passing above it. Tx–Rx is a moving transmitter–receiver system.

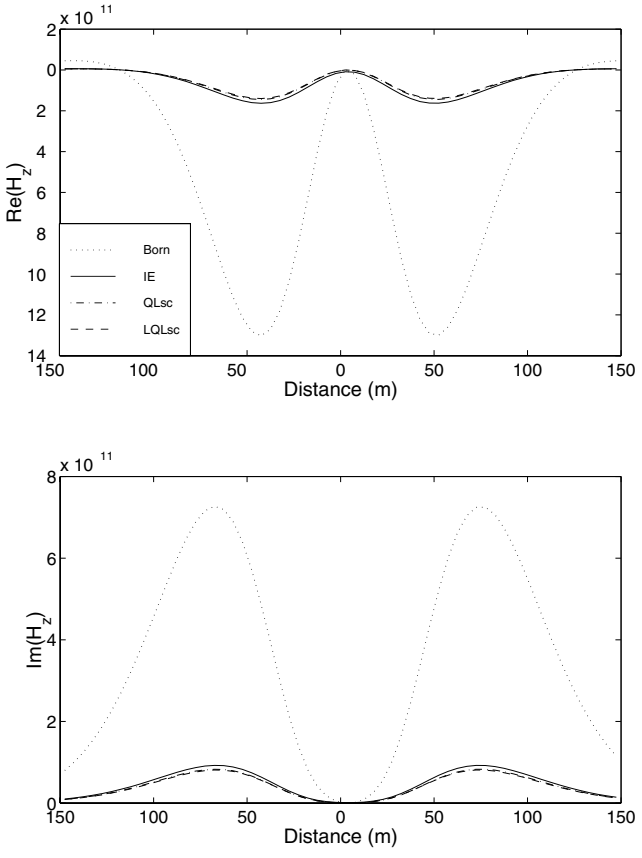

Figure 4. Numerical comparison of full IE solution (IE), Born approximation (Born), scalar QL approximation (QLsc), and scalar LQL approximation (LQLsc) at frequency $f=56$ kHz for Model 2 (Fig. 3). The real and imaginary parts of the vertical component of the anomalous magnetic field are presented at receivers along the Y-axis at a height of 30 m above the ground.

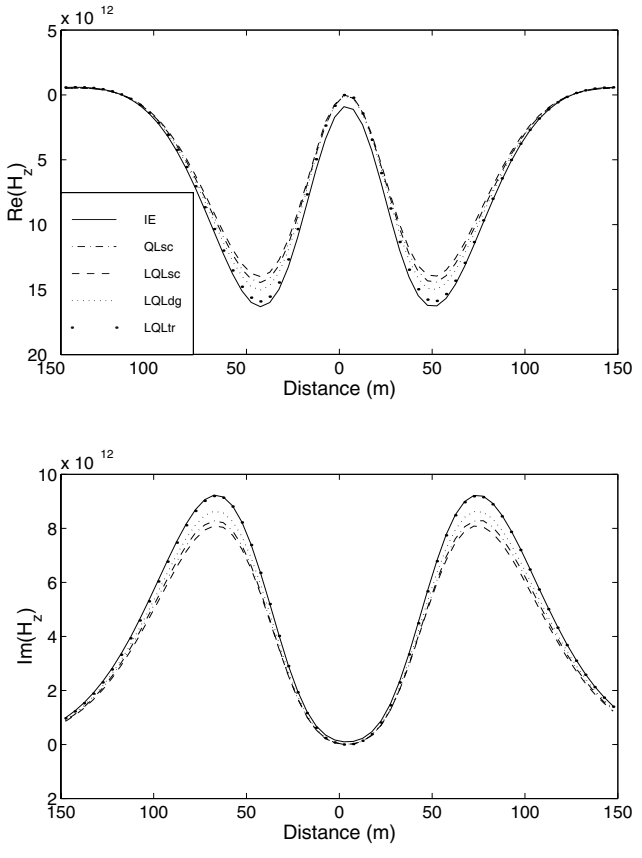

Figure 5. Numerical comparison of full IE solution (IE), scalar QL approximation (QLsc), scalar LQL approximation (LQLsc), diagonal LQL approximation (LQLdg) and tensor LQL approximation (LQLtr), at frequency $f=56$ kHz for Model 2 (Fig. 3). The real and imaginary parts of the vertical component of the anomalous magnetic field are presented at receivers along the Y-axis at a height of 30 m above the ground.

Following Zhdanov & Fang (1996b, 1999), we introduce a new tensor function

$$\widehat{\boldsymbol{m}}(\mathbf{r}) = \Delta\tilde{\sigma}(\mathbf{r})\left[\hat{\boldsymbol{I}} + \hat{\boldsymbol{\lambda}}_{\mathrm{L}}(\mathbf{r})\right], \tag{27}$$

which we call a modified material property tensor. Note that this tensor function is independent of the transmitter position, because $\hat{\boldsymbol{\lambda}}_{\mathrm{L}}$ does not depend on the background field. This is the main difference between the localized QL inversion and the original QL inversion (Zhdanov & Fang 1999). Eqs (16) and (17) take the forms

$$\mathbf{E}^{\mathrm{a}}_{\mathrm{LQL}}(\mathbf{r}_j) = \mathbf{G}_{\mathbf{E}}\left(\widehat{\boldsymbol{m}}(\mathbf{r})\mathbf{E}^{\mathrm{b}}(\mathbf{r})\right) \tag{28}$$

and

$$\mathbf{H}^{\mathrm{a}}_{\mathrm{LQL}}(\mathbf{r}_j) = \mathbf{G}_{\mathbf{H}}\left(\widehat{\boldsymbol{m}}(\mathbf{r})\mathbf{E}^{\mathrm{b}}(\mathbf{r})\right). \tag{29}$$

We assume now that the anomalous parts of the electric, $\mathbf{E}^{\mathrm{a}}(\mathbf{r}_j)$, and/or magnetic, $\mathbf{H}^{\mathrm{a}}(\mathbf{r}_j)$, fields (generated by a transmitter with one or several different positions) are measured in a number of the observation points, $\mathbf{r}_j$. Using the LQL approximation for the observed fields, $\mathbf{d}$, we arrive at the following equation:

$$\mathbf{d} = \mathbf{G}_{\mathbf{d}}\left(\widehat{\boldsymbol{m}}(\mathbf{r})\mathbf{E}^{\mathrm{b}}(\mathbf{r})\right), \tag{30}$$

which is linear with respect to the material property tensor $\widehat{\boldsymbol{m}}(\mathbf{r})$. In this equation, $\mathbf{d}$ denotes the electric or the magnetic field, $\mathbf{E}$ or $\mathbf{H}$, and $\mathbf{G}_{\mathbf{d}}$ denote operator $\mathbf{G}_{\mathbf{E}}$ or $\mathbf{G}_{\mathbf{H}}$, respectively. We can solve the linear equation (30) with respect to $\widehat{\boldsymbol{m}}(\mathbf{r})$, which is source-independent. Now, based on condition (15), we can determine $\hat{\boldsymbol{\lambda}}(\mathbf{r})$ from the equation

$$\hat{\boldsymbol{\lambda}}_{\mathrm{L}}(\mathbf{r}) = \mathbf{G}_{\mathbf{E}}(\widehat{\boldsymbol{m}}(\mathbf{r})). \tag{31}$$

Knowing $\hat{\boldsymbol{\lambda}}_{\mathrm{L}}(\mathbf{r})$ and $\widehat{\boldsymbol{m}}(\mathbf{r})$, similar to the QL inversion scheme, we can find $\Delta\tilde{\sigma}(\mathbf{r})$ from eq. (27). Note that eq. (27) should hold for any frequency, because the electrical reflectivity tensor and the material property tensor are functions of frequency as well: $\hat{\boldsymbol{\lambda}}_{\mathrm{L}} = \hat{\boldsymbol{\lambda}}_{\mathrm{L}}(\mathbf{r}, \omega)$, $\widehat{\boldsymbol{m}} = \widehat{\boldsymbol{m}}(\mathbf{r}, \omega)$. In reality, of course, it holds only approximately. Therefore, the conductivity $\Delta\tilde{\sigma}(\mathbf{r})$ can be found by using the least-squares method of solving eq. (27):

$$\left\|\widehat{\boldsymbol{m}}(\mathbf{r}, \omega) - \Delta\tilde{\sigma}(\mathbf{r})\left[\hat{\boldsymbol{I}} + \hat{\boldsymbol{\lambda}}_{\mathrm{L}}(\mathbf{r}, \omega)\right]\right\|_{L_2(\omega)} = \min. \tag{32}$$

This inversion scheme can be used for multisource techniques, because $\boldsymbol{\lambda}_{\mathrm{L}}$ and $\widehat{\boldsymbol{m}}$ are source-independent. Similar to Zhdanov & Fang (1996b) and Torres-Verdin & Habashy (1995), it reduces the original non-linear inverse problem to three linear inverse problems: the first one (the quasi-Born inversion) for the parameter $\widehat{\boldsymbol{m}}$, another one for the parameter $\hat{\boldsymbol{\lambda}}$, and the third one (a correction of the result for quasi-Born inversion) for the conductivity $\Delta\tilde{\sigma}$.

Note that the modified material property tensor $\hat{\boldsymbol{m}}$ has a similar physical meaning to the anomalous currents, and it is found through a quasi-Born-type, linear inversion. We can rewrite eq. (30) using matrix notation:

$$\mathbf{d} = \hat{\mathbf{G}}\,\mathbf{m}\,. \tag{33}$$

Here $\mathbf{m}$ is the vector-column of the modified material property tensor $\hat{\boldsymbol{m}}$, $\mathbf{d}$ is the vector-column of the field data, and the matrix $\hat{\mathbf{G}}$ is the matrix of the linear operator defined by eq. (30). Similarly, we can obtain from eq. (31)

$$\hat{\boldsymbol{\lambda}} = \hat{\mathbf{G}}^E\mathbf{m}\,, \tag{34}$$

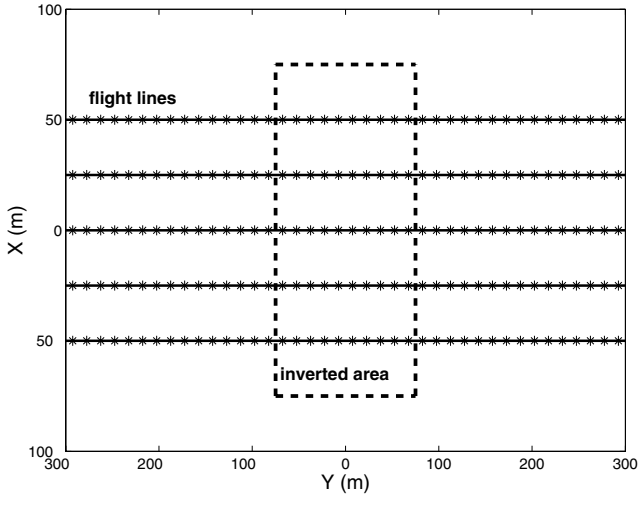

Figure 6. Schematic plan view of survey configuration and inverted area for Model 3 (Fig. 8 top panel).

where $\hat{\boldsymbol{\lambda}}$ is a block-diagonal matrix of reflectivity tensors and $\hat{\mathbf{G}}^E$ denotes a matrix of the linear operator defined by expression (5) with the electric Green's tensor.

The solution of the inverse problem is reduced to the inversion of the linear system (33) with respect to $\mathbf{m}$ and then to computing $\hat{\boldsymbol{\lambda}}$ using eq. (34). After that, we find $\Delta\tilde{\boldsymbol{\sigma}}$ as a least-squares solution of the optimization problem (32).

We use the regularized conjugate gradient (RCG) method to solve the system of the linear eq. (30). The RCG algorithm is described in the Appendix.

4.1 Scalar reflectivity tensor

In the case of a scalar reflectivity tensor, we introduce a scalar parameter $m(\mathbf{r})$:

$$m(\mathbf{r}) = \Delta\tilde{\sigma}(\mathbf{r})[1 + \lambda_{\mathrm{L}}(\mathbf{r})]\,. \tag{35}$$

Eq. (30) simplifies to

$$\mathbf{d} = \mathbf{G}_{\mathbf{d}}\big(m(\mathbf{r})\mathbf{E}^{\mathrm{b}}(\mathbf{r})\big)\,. \tag{36}$$

A scalar reflectivity coefficient $\lambda_{\mathrm{L}}(\mathbf{r})$ is determined, based on the condition (21),

$$\big\|\lambda_{\mathrm{L}}(\mathbf{r}_j)\hat{\boldsymbol{I}} - \mathbf{G}_{\mathbf{E}}(m(\mathbf{r}))\big\|_{L_2(D)} = \min\,.$$

The electrical conductivity is found as the least-squares solution of the minimization problem

$$\|m(\mathbf{r},\,\omega) - \Delta\tilde{\sigma}(\mathbf{r})[1 + \lambda_{\mathrm{L}}(\mathbf{r},\,\omega)]\|_{L_2(\omega)} = \min\,. \tag{37}$$

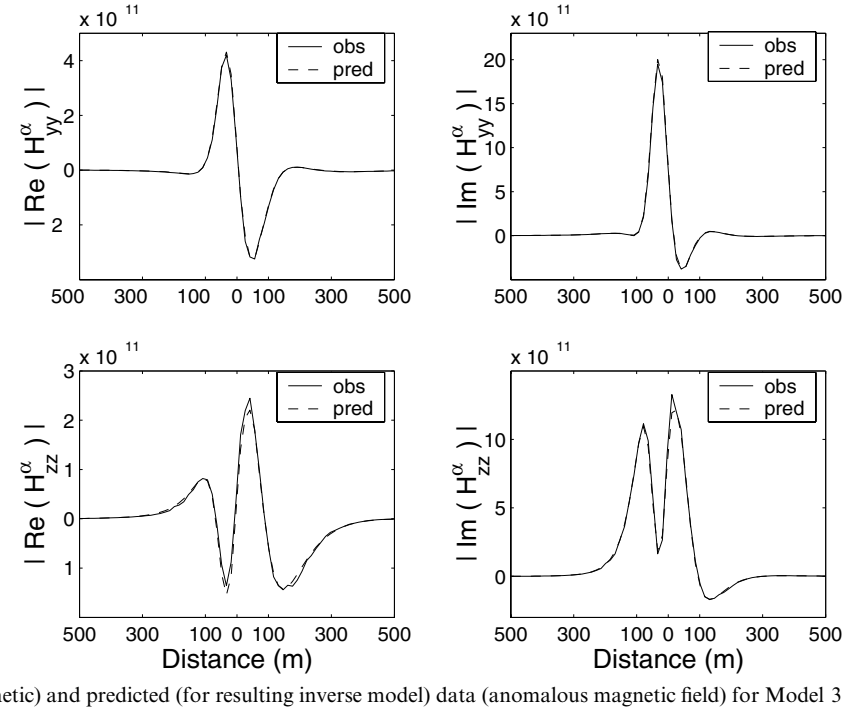

Figure 7. Observed (synthetic) and predicted (for resulting inverse model) data (anomalous magnetic field) for Model 3 (Fig. 8 top panel). Data for 900 Hz are shown.

4.2 Diagonal reflectivity tensor

In the case of the diagonal reflectivity tensor, $\hat{\lambda}_{\mathrm{L}} = \mathrm{diag}\ \lambda_{\mathrm{L}}$, we introduce a diagonal material property tensor

$$\widehat{m} = \mathrm{diag}\,\mathbf{m} = \begin{bmatrix} m_x & 0 & 0 \\ 0 & m_y & 0 \\ 0 & 0 & m_z \end{bmatrix}, \tag{38}$$

according to the equation

$$\mathrm{diag}\,\mathbf{m}(\mathbf{r}) = \Delta\tilde{\sigma}(\mathbf{r})\left[\hat{I} + \mathrm{diag}\,\boldsymbol{\lambda}_{\mathrm{L}}(\mathbf{r})\right], \tag{39}$$

where $\mathbf{m}$ is a material property vector:

$$\mathbf{m} = \begin{bmatrix} m_x \\ m_y \\ m_z \end{bmatrix}. \tag{40}$$

Eq. (30) takes the form

$$\mathbf{d} = \mathbf{G}_{\mathbf{d}}\left(\mathrm{diag}\,\mathbf{m}(\mathbf{r})\mathbf{E}^{\mathrm{b}}(\mathbf{r})\right). \tag{41}$$

The reflectivity vector $\boldsymbol{\lambda}_{\mathrm{L}}(\mathbf{r})$ is determined, based on the condition (26):

$$\left\|\mathrm{diag}\,\boldsymbol{\lambda}_{\mathrm{L}}(\mathbf{r}_j) - \mathbf{G}_{\mathbf{E}}(\mathrm{diag}\,\mathbf{m}(\mathbf{r}))\right\|_{L_2(D)} = \min. \tag{42}$$

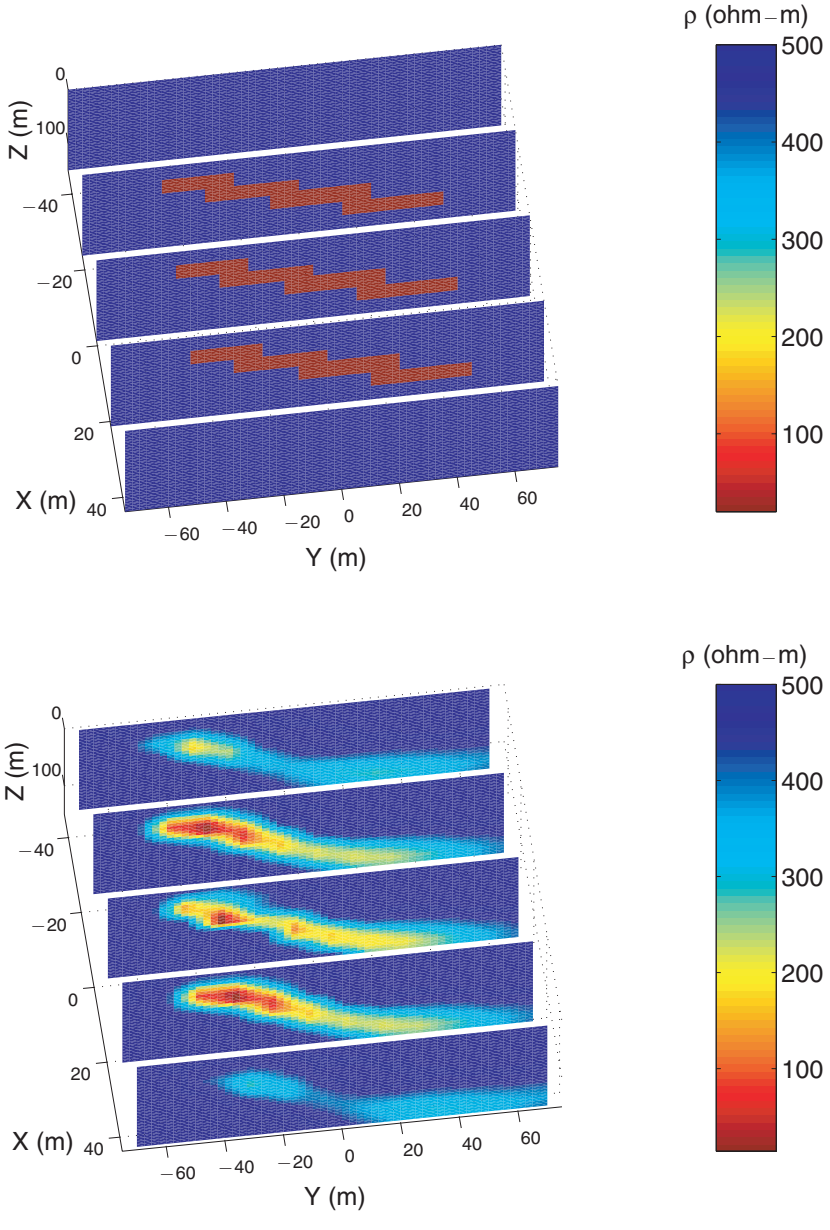

Figure 8. Successive resistivity cross-sections through the 3-D geoelectric model of a conductive, dipping dike in a homogeneous half-space (top panel), and the corresponding LQL inversion result (bottom panel).

And, finally, the electrical conductivity is found as the least-squares solution of the minimization problem

$$\left\| \operatorname{diag} \mathbf{m}(\mathbf{r}, \omega) - \Delta\tilde{\sigma}(\mathbf{r}) \left[\hat{\boldsymbol{I}} + \operatorname{diag} \boldsymbol{\lambda}_{\mathrm{L}}(\mathbf{r}, \omega) \right] \right\|_{L_2(\omega)} . \tag{43}$$

4.3 Choice of the type of electrical reflectivity tensor used in the LQL inversion scheme

As we demonstrated through numerical examples in the previous section, the LQL approximation is increasingly more accurate, as we use more complex electrical reflectivity tensors (scalar, diagonal and full tensors). The choice, however, of the appropriate type of electrical reflectivity tensor in the LQL inversion scheme requires further analysis.

First, we should take into account the trade-off between accuracy and memory requirements. A scalar reflectivity tensor means that we only need to invert for one parameter per cell of the anomalous domain. This number is tripled when we use a diagonal reflectivity tensor, and for a full reflectivity tensor, we have nine times that number. This represents a considerable increase in computation in most cases, since a major slowdown in computation speed happens when the required memory exceeds the physical memory of the computer.

Another limitation we encounter in the inversion process is the limited number of EM field components that are usually available. Helicopter-borne EM (HEM) surveys, for example, normally employ two survey configurations: a horizontal coplanar coil pair, which measures the H_{zz} component, and a vertical coaxial coil pair, which measures the H_{yy} component.

Let us recall eq. (29) for the anomalous magnetic field. In discretized form the above equation becomes

$$\mathbf{H}^{ij} = \sum_{k=1}^{N} \hat{\Gamma}^{kj} \hat{m}^k \mathbf{E}^{ik} , \tag{44}$$

where N is the number of cells in the anomalous domain, the index i denotes the ith transmitter, and the index j denotes the jth receiver. Using tensor notation, the α component of the magnetic field (where $\alpha = x, y, z$) is given by

$$\begin{aligned} H_{\alpha}^{ij} = \sum_{k=1}^{N} \Gamma_{\alpha\beta}^{kj} m_{\beta\gamma}^{k} E_{\gamma}^{ik} = \sum_{k=1}^{N} \big[& \Gamma_{\alpha x}^{kj} m_{xx}^{k} E_{x}^{ik} + \Gamma_{\alpha x}^{kj} m_{xy}^{k} E_{y}^{ik} \\ & + \Gamma_{\alpha x}^{kj} m_{xz}^{k} E_{z}^{ik} + \Gamma_{\alpha y}^{kj} m_{yx}^{k} E_{x}^{ik} + \Gamma_{\alpha y}^{kj} m_{yy}^{k} E_{y}^{ik} + \Gamma_{\alpha y}^{kj} m_{yz}^{k} E_{z}^{ik} \\ & + \Gamma_{\alpha z}^{kj} m_{zx}^{k} E_{x}^{ik} + \Gamma_{\alpha z}^{kj} m_{zy}^{k} E_{y}^{ik} + \Gamma_{\alpha z}^{kj} m_{zz}^{k} E_{z}^{ik} \big] . \end{aligned} \tag{45}$$

For a z-directed dipole transmitter, $\Gamma_{\alpha z} = \Gamma_{zz} = 0$ (by definition), and $E_z = 0$ (no vertical component of the electric field is induced in a 1-D earth). Thus

$$H_{z}^{ij} = \sum_{k=1}^{N} \left[\Gamma_{zx}^{kj} m_{xx}^{k} E_{x}^{ik} + \Gamma_{zx}^{kj} m_{xy}^{k} E_{y}^{ik} + \Gamma_{zy}^{kj} m_{yx}^{k} E_{x}^{ik} + \Gamma_{zy}^{kj} m_{yy}^{k} E_{y}^{ik} \right] , \tag{46}$$

which means that we can only resolve four (m_{xx}, m_{xy}, m_{yx} and m_{yy}) of the nine components of the material property tensor.

For a y-directed dipole transmitter located in the air, $E_z = 0$ (no vertical component of the electric field is induced in the earth, because of the very high resistivity contrast at the air–earth interface). Thus

$$\begin{aligned} H_{y}^{ij} = \sum_{k=1}^{N} \big[& \Gamma_{yx}^{kj} m_{xx}^{k} E_{x}^{ik} + \Gamma_{yx}^{kj} m_{xy}^{k} E_{y}^{ik} + \Gamma_{yy}^{kj} m_{yx}^{k} E_{x}^{ik} \\ & + \Gamma_{yy}^{kj} m_{yy}^{k} E_{y}^{ik} + \Gamma_{yz}^{kj} m_{zx}^{k} E_{x}^{ik} + \Gamma_{yz}^{kj} m_{zy}^{k} E_{y}^{ik} \big] , \end{aligned} \tag{47}$$

which means that we can only resolve six (m_{xx}, m_{xy}, m_{yx}, m_{yy}, m_{zx}, m_{zy}) of the nine components of the material property tensor.

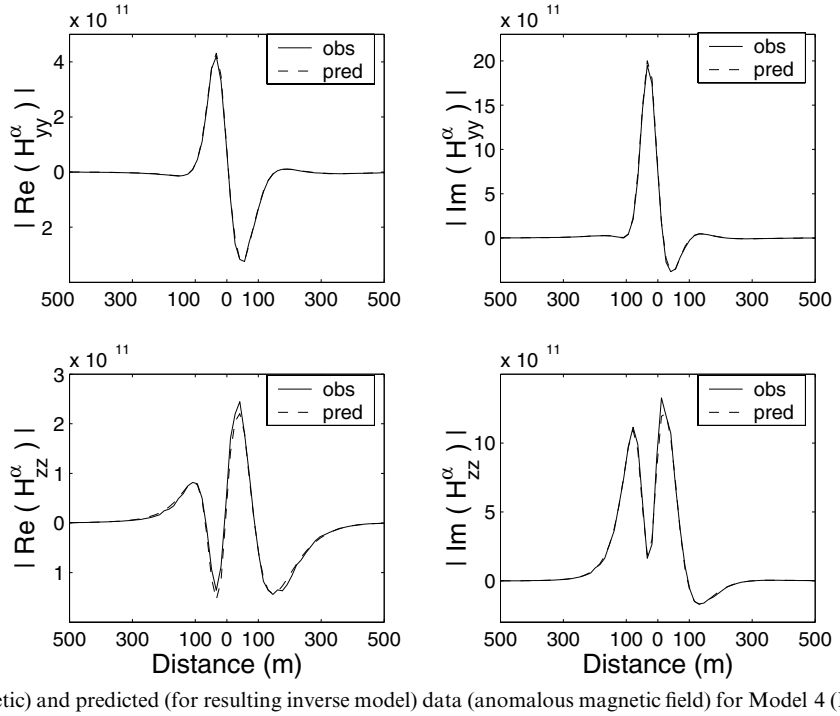

Figure 9. Observed (synthetic) and predicted (for resulting inverse model) data (anomalous magnetic field) for Model 4 (Fig. 10 top panel). Data for 900 Hz are shown.

The above analysis shows that in most situations we cannot recover the full material property tensor (and hence, the reflectivity tensor either). Also considering the computer memory issues we discussed above, as well as the fact that using a full tensor renders the inverse problem underdetermined, we conclude that for all practical purposes the use of scalar reflectivity and material property tensors in the inverse problem solution is sufficient.

Use of a more complex tensor could be justified when data from new-generation, multicomponent geophysical equipment becomes available in the future.

5 3-D INVERSION OF SYNTHETIC HELICOPTER-BORNE DATA BASED ON THE LQL APPROXIMATION

One of the most important possible applications of the LQL inversion technique is the interpretation of frequency-domain HEM data. This type of airborne survey is used extensively in mineral exploration. We employed the integral equation code SYSEM (Xiong 1992) to simulate such a survey over a conductive (20 Ω m) dipping dike located in a resistive (500 Ω m) half-space. Five survey lines were flown over the target at an altitude of 30 m and at a distance of 25 m from each other. A schematic plan view of the survey is shown in Fig. 6.

The moving transmitter–receiver system was a pair of vertical magnetic dipoles (simulating a horizontal coplanar coil pair), and a pair of horizontal magnetic dipoles (simulating a vertical coaxial coil pair), with 8 m horizontal separation. The *yy* (coaxial) and *zz* (coplanar) components of the anomalous magnetic field were measured every 15 m along the lines (70 observation points in each line). Two frequencies were used: 900 Hz and 7.2 kHz.

We added 5 per cent random noise to the anomalous magnetic field and then inverted it using the LQL inversion method with a scalar reflectivity tensor and a focusing inverse imaging (see the Appendix). The inverted area, centred around the body, was 150 m × 150 m × 150 m, and was divided into 12 × 12 × 12 cells. Fig. 7 shows the comparison of observed (synthetic) and predicted (for the resulting inverse model) data for the central profile passing above the centre of the dike. The predicted data fit the observed data very well (the inversion was stopped as soon as the misfit reached the 5 per cent noise level).

Fig. 8 shows successive resistivity cross-sections through the true model (top panel) and the inverted volume (bottom panel). Both the location and the depth of the dike are determined very well. Its dip is also remarkably well defined. We can even distinguish some of the details of its shape. Its resistivity, however, is overestimated. These results demonstrate the stability of the method in the presence of noise (results of inversion of noise-free data are very similar but not shown here). Moreover, the method is very fast, with the 3-D inversion for 350 total different transmitter–receiver pairs, two frequencies and two components, requiring approximately 1 hr of CPU time on an Ultra Sparc 10 station at 440 MHz.

The second model we have used in this study consists of a resistive (1000 Ω m) and a conductive (10 Ω m) body embedded in a host of resistivity 100 Ω m. We simulated the same helicopter-borne EM survey as above.

The synthetic data were again contaminated with 5 per cent random noise and then inverted using the LQL inversion method. Fig. 9 shows the comparison of observed (synthetic) and predicted (for the resulting inverse model) data for the central profile. The predicted data fit the observed data very well (within the 5 per cent noise level). The 3-D images of the true model and the inversion result are shown in Fig. 10. We can clearly locate the two anomalies. The resistive body is located at the correct position, while the conductive body is imaged a little deeper than it should be. The resistivity contrasts

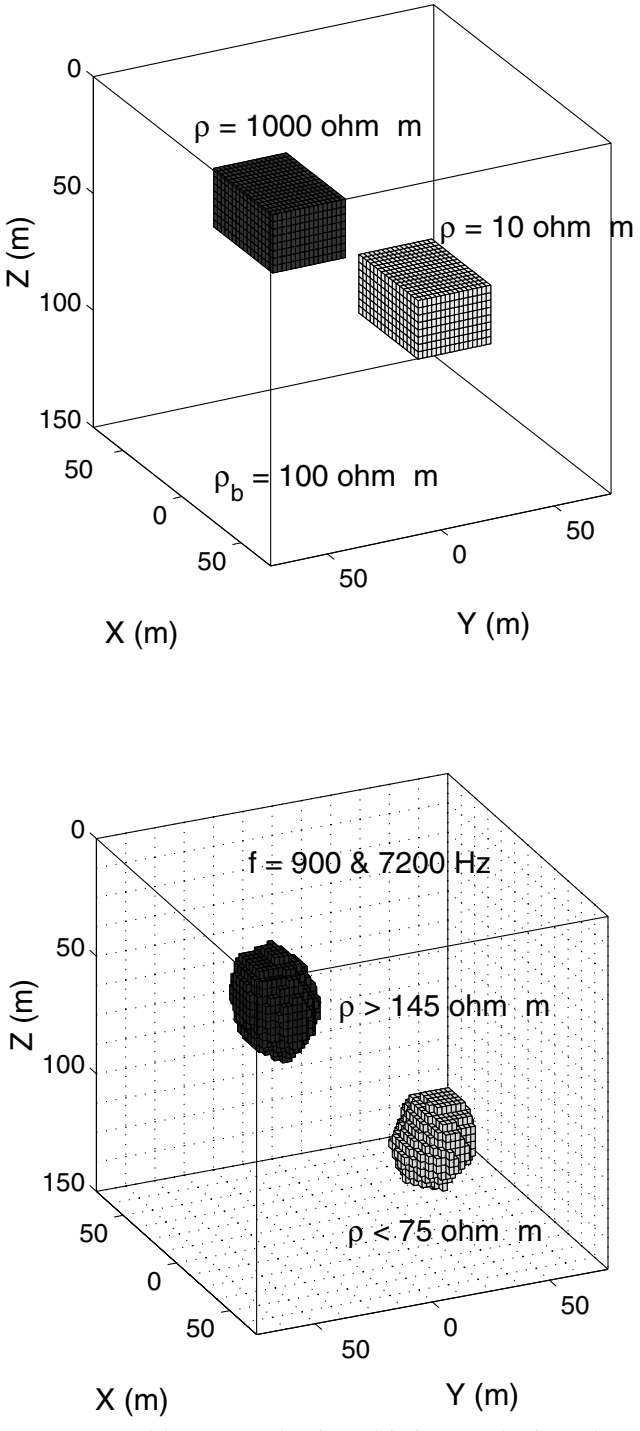

Figure 10. Model 4: 3-D geoelectric model of one conductive and one resistive rectangular inclusion in a homogeneous half-space (top panel), and 3-D image of the LQL inversion result (bottom panel).

of both anomalies with the background are underestimated. The results are not perfect but, considering the non-linearity of the specific problem (conductive and resistive anomalies close to each other), they are quite satisfactory. The CPU time required was similar to that of the previous model.

6 3-D LQL INVERSION OF HEM DATA COLLECTED FOR MINERAL EXPLORATION AT VOISEY'S BAY, LABRADOR, CANADA

The Voisey's Bay area in Labrador, Canada, is characterized by high-conductivity Ni–Cu–Co sulphide deposits hosted by resistive troctolite dikes (Naldrett *et al.* 1996). There are several identified deposits as shown in Fig. 11. Several types of ground and airborne geophysical surveys have been conducted in the Voisey's Bay area, including gravity, magnetic, magnetotelluric, time-domain EM and HEM surveys. An HEM data set was provided to us by INCO Exploration. It consists of several flight lines that cover the entire area. The deposits on the eastern part of the survey area, however, are too deep to be detected by the HEM, which can only penetrate down to a depth of approximately 150 m. We have, therefore, chosen to invert the data from the central part of the area (outlined in Fig. 11) that corresponds to the location of the Ovoid deposit. This flat-lying, high-conductance deposit is located under 20 m of overburden and comprises 70 per cent massive sulphide (Balch *et al.* 1998).

The data were collected with the standard Dighem HEM system (Fraser 1972, 1979, 1981), which consists of a horizontal coplanar and a vertical coaxial coil pair. Based on drilling information incorporated in Fig. 11, and following a simple 1-D modelling of the data that are far away from any known deposits, we have assumed a 1-D resistivity background consisting of a 20 m deep, conductive overburden with a resistivity of 10 Ω m, and a lower half-space with a resistivity of 1900 Ω m. We used the coplanar (CP) and coaxial (CX) components from the lowest available frequency (900 Hz), which is the least sensitive to the presence of the conductive overburden. The data were first interpolated along a uniform (in each direction) grid and then transformed from ppm to anomalous field values. The data comprise part of four flight lines, at a distance of 200 m from each other. The inverted area was 700 m $\times$ 600 m $\times$ 160 m, and was divided into $14 \times 30 \times 8$ cells (Fig. 12).

After the described data processing, we inverted the data using a scalar reflectivity tensor. Owing to the complexity of the

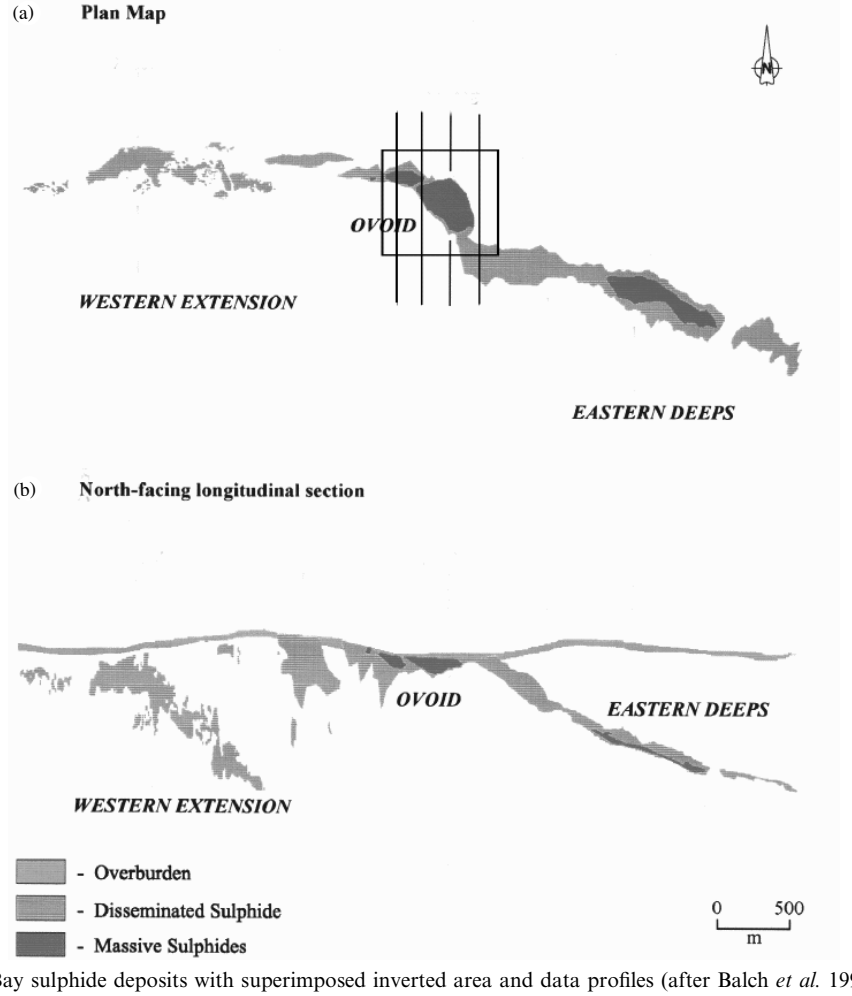

Figure 11. The Voisey's Bay sulphide deposits with superimposed inverted area and data profiles (after Balch *et al.* 1998).

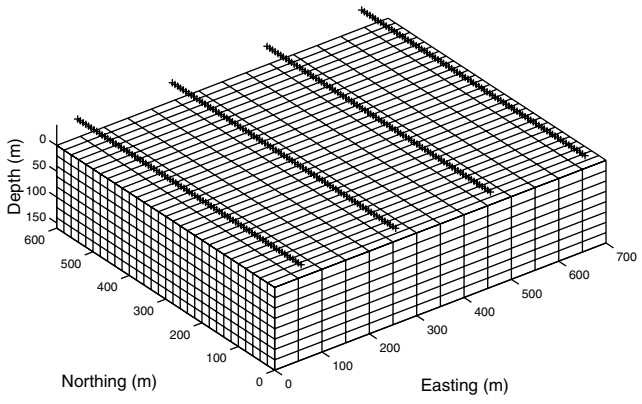

Figure 12. 3-D inverted volume with grid subdivision and superimposed flight lines location.

target and its large size (meaning that most of the cells in the inverted area are likely to have some anomalous conductivity), we did not use focused imaging, but a simple minimum norm stabilizer.

The LQL inversion was terminated when the misfit reached 3 per cent. The 3-D (simultaneous) inversion of 332 data points (corresponding to 332 different transmitter–receiver positions) required approximately 25 min of CPU time on an Ultra Sparc 10 station at 440 MHz (this computation time includes the calculation of the electric Green's tensor in the anomalous domain; the actual minimization routine requires approximately 20 s). Fig. 13 shows the observed and predicted data along the second and third profiles, where the largest anomalies occur. The agreement is very good.

Fig. 14 shows the inversion results for the CP (middle panel) and CX (bottom panel) components in the form of successive cross-sections through the inverted volume. The top panel of the figure shows the horizontal extent of the sulphides in the inverted area, as can be inferred from Fig. 11. The results of the LQL inversion are geologically reasonable and in very good agreement with the existing information concerning the Ovoid deposit. In particular, a large elongated conductive body is located approximately at the centre of the inverted area. The body is extended towards the SE and the W–NW. The reliability of these results is enhanced

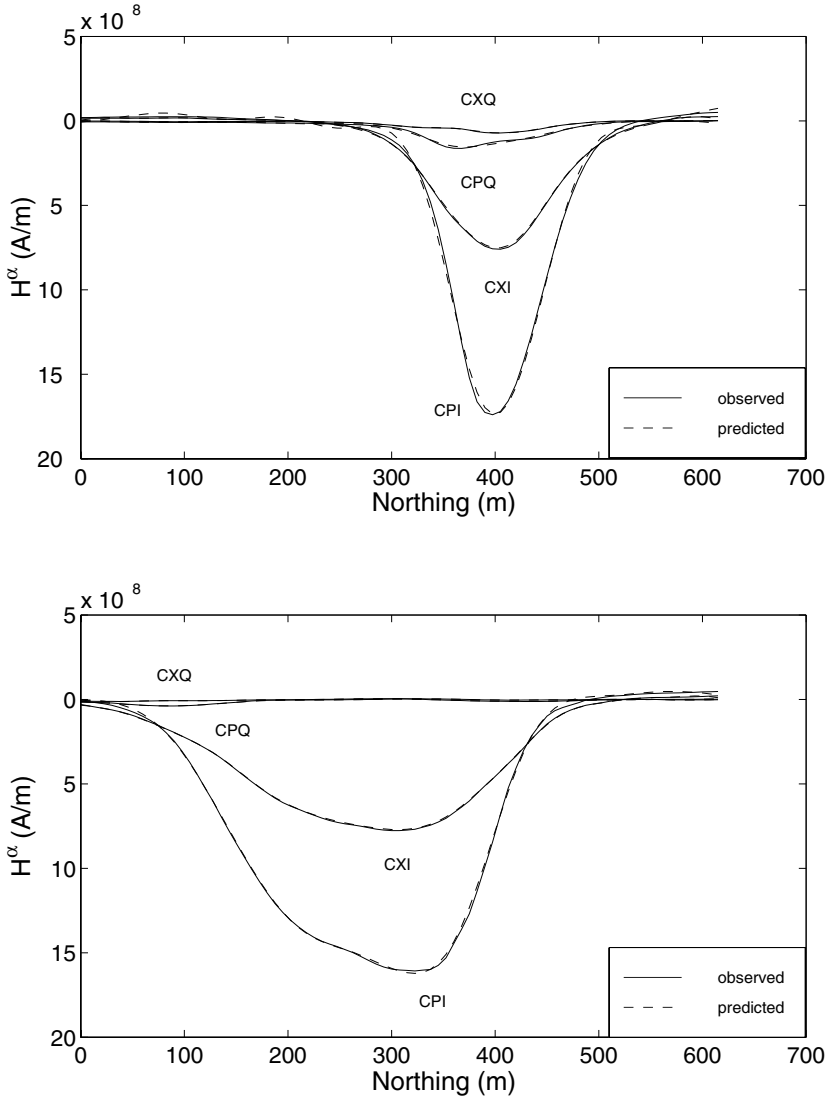

Figure 13. Observed (solid line) and predicted (dashed line) data along the second (top panel) and third (bottom panel) inverted profiles. The coplanar in-phase (CPI), coplanar quadrature (CPQ), coaxial in-phase (CXI) and coaxial quadrature (CXQ) components are shown.

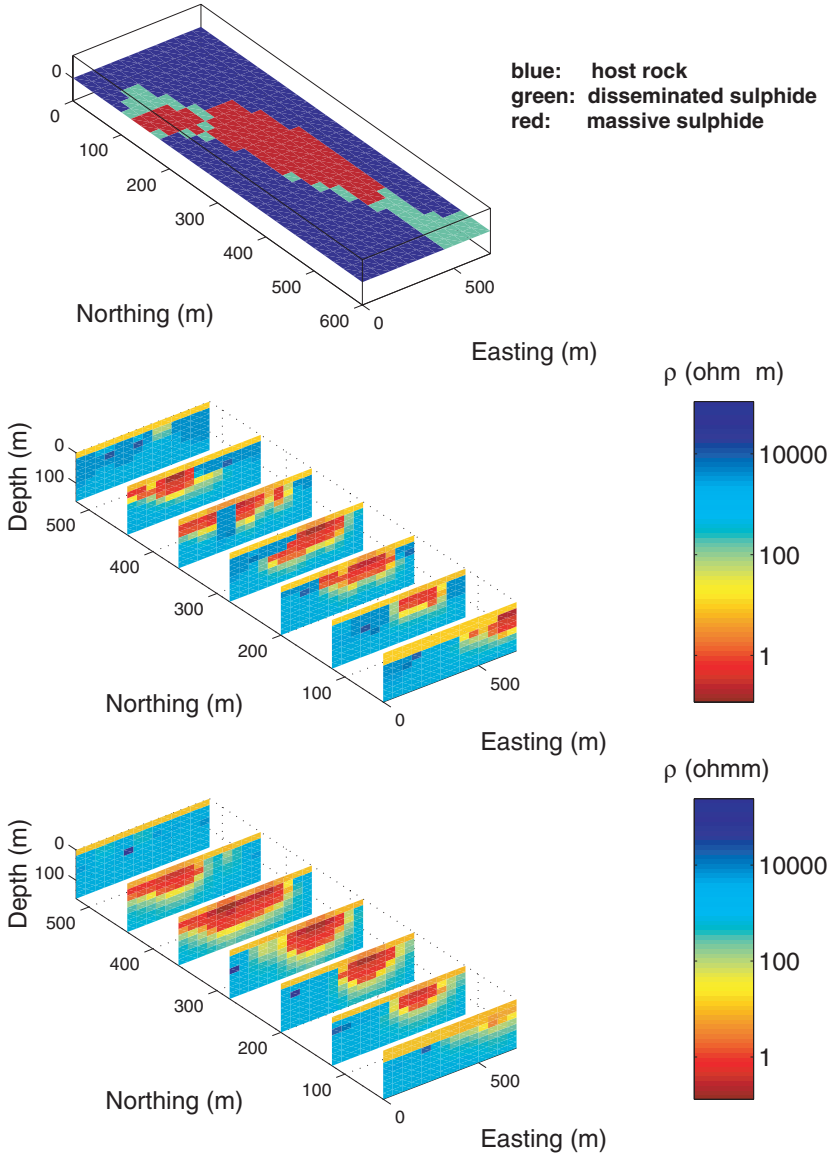

Figure 14. Horizontal extent of the sulphides in the inverted area as inferred from Fig. 11 (top panel), and cross-sections of the inverted volume for the coplanar (middle panel) and the coaxial (bottom panel) components.

by the fact that, despite small differences, inversion results for the two different components, agree quite well with each other. We should finally mention that our results agree remarkably well with the image obtained by Oldenburg *et al.* (1998) as a result of their 3-D gravity inversion over the same area.

7 CONCLUSIONS

We have developed a localized quasi-linear approximation that is source-independent. This LQL approximation provides a practical solution to the problem of 3-D inversion of multi-transmitter frequency-domain EM data. This is of utmost importance for geophysical applications, such as airborne EM, well logging and cross-well imaging.

We have also developed a 3-D inversion scheme based on the LQL approximation. We have used this method to invert synthetic data simulating an HEM survey over two different models. The results are very good and demonstrate the stability and efficiency of the method. We have also inverted HEM data collected by INCO Exploration over the Voisey's Bay deposit in Canada. The results successfully delineate the massive sulphides and show that the method can be used in complex geological environments. More research is needed, however, in order to establish the validity of the method in different geophysical applications.

ACKNOWLEDGMENTS

This material is based in part upon work supported by the National Science Foundation under Grant No 9987779. The authors also acknowledge the support of the University of Utah Consortium for Electromagnetic Modeling and Inversion (CEMI), which includes Advanced Power Technologies Inc., AGIP, Baker Atlas Logging Services, BHP Minerals, EXXON–MOBIL Upstream Research Company, INCO Exploration,

Japan National Oil Corporation, MINDECO, Naval Research Laboratory, Rio Tinto-Kennecott, 3JTech Corporation, and Zonge Engineering.We especially want to thank INCO Exploration for providing the excellent HEM data set from Voisey's Bay and allowing us to publish these results. We would also like to thank Gabor Hursan for his help with the focusing RCG inversion routine. Finally, we want to thank two anonymous reviewers for their useful comments and suggestions on our original manuscript.

REFERENCES

Balch, S.J., Crebs, T.J., King, A. & Verbiski, M., 1998. Geophysics of the Voisey's Bay Ni–Cu–Co deposits, *68th Annual International Meeting, Soc. of Expl. Geophys., Expanded Abstracts,* pp. 784–787.

Dmitriev, V.I. & Pozdnyakova, E.E., 1992. Method and algorithm for computing the electromagnetic field in a stratified medium with a local inhomogeneity in an arbitrary layer, *Comput. Math.,* **3,** 181–188.

Fraser, D.C., 1972. A new multicoil aerial electromagnetic prospecting system, *Geophysics,* **37,** 518–537.

Fraser, D.C., 1979. The multicoil II airborne electromagnetic system, *Geophysics,* **44,** 1367–1394.

Fraser, D.C., 1981. Magnetite mapping with a multicoil airborne electromagnetic system, *Geophysics,* **46,** 1579–1593.

Habashy, T.M., Groom, R.W. & Spies, B.R., 1993. Beyond the Born and Rytov approximations: a nonlinear approach to electromagnetic scattering, *J. geophys. Res.,* **98,** 1759–1775.

Hohmann, G.W., 1975. Three-dimensional induced polarization and EM modeling, *Geophysics,* **40,** 309–324.

Naldrett, A.J., Keats, H., Sparkes, K. & Moore, S., 1996. Geology of the Voisey's Bay Ni–Cu–Co deposit, Labrador, Canada, *Explor. Mining Geol.,* **5,** 169–179.

Oldenburg, D.W., Li, Y., Farquharson, C.G., Kowalczyk, P., Aravanis, T., King, A., Zhang, P. & Watts, A., 1998. Applications of geophysical inversions in mineral exploration, *The Leading Edge,* **17,** 461–465.

Portniaguine, O. & Zhdanov, M.S., 1999. Focusing geophysical inversion images, *Geophysics,* **64,** 874–887.

Tikhonov, A.N. & Arsenin, V.Y., 1977. *Solution of Ill-Posed Problems,* Winston, Washington, DC.

Torres-Verdin, C. & Habashy, T.M., 1994. Rapid 2.5-dimensional forward modeling and inversion via a new nonlinear scattering approximation, *Radio Science,* **29,** 1051–1079.

Torres-Verdin, C. & Habashy, T.M., 1995. A two-step linear inversion of two-dimensional electrical conductivity, *IEEE Trans. Antenn. Propag.,* **43,** 405–415.

Weidelt, P., 1975. EM induction in three-dimensional structures, *J. Geophysics,* **41,** 85–109.

Xiong, Z., 1992. EM modeling of three-dimensional structures by the method of system iteration using integral equations, *Geophysics,* **57,** 1556–1561.

Zhdanov, M.S., 1993. *Tutorial: Regularization in Inversion Theory,* Colorado School of Mines.

Zhdanov, M.S., 2002. *Geophysical Inverse Theory and Regularization Problems,* Elsevier, Amsterdam.

Zhdanov, M.S. & Fang, S., 1996a. Quasi-linear approximation in 3D EM modeling, *Geophysics,* **61,** 646–665.

Zhdanov, M.S. & Fang, S., 1996b. 3-D quasi-linear electromagnetic inversion, *Radio Sci.,* **31,** 741–754.

Zhdanov, M.S. & Fang, S., 1997. Quasi linear series in 3D EM modeling, *Radio Sci.,* **32,** 2167–2188.

Zhdanov, M.S. & Fang, S., 1999. 3D quasi-linear electromagnetic modeling and inversion, in *Three Dimensional Electromagnetics, SEG Monograph,* pp. 233–255.

Zhdanov, M.S. & Hursan, G., 2000. 3-D electromagnetic inversion based on quasi-analytical approximation, *Inverse Problems,* **16,** 1297–1322.

Zhdanov, M.S. & Keller, G., 1994. *The Geoelectrical Methods in Geophysical Exploration,* Elsevier, Amsterdam.

Zhou, C. & Liu, L., 2000. Radar-diffraction tomography using the modified quasi-linear approximation, *IEEE Trans. Geosci. Remote Sensing,* **38,** 404–415.

APPENDIX A: REGULARIZED SOLUTION OF THE LINEAR INVERSE PROBLEM FOR THE MATERIAL PROPERTY TENSOR

The linear inverse problem (33) is ill-posed, i.e. the solution can be non-unique and unstable. The conventional way of solving ill-posed inverse problems according to regularization theory (Tikhonov & Arsenin 1977; Zhdanov & Keller 1994) is based on the minimization of the Tikhonov parametric functional

$$P^{\alpha}(\mathbf{m}) = \phi(\mathbf{m}) + \alpha S(\mathbf{m}) = \min\,, \tag{A1}$$

where the misfit functional is specified as

$$\phi(\mathbf{m}) = \left\| \widehat{\mathbf{W}}_d \left(\widehat{\mathbf{G}}\mathbf{m} - \mathbf{d} \right) \right\|^2, \tag{A2}$$

the stabilizer is selected to be equal to

$$S(\mathbf{m}) = \|\widehat{\mathbf{W}}_m(\mathbf{m} - \mathbf{m}_{\rm apr})\|^2, \tag{A3}$$

where α is the regularization parameter, and $\widehat{\mathbf{W}}_d$ and $\widehat{\mathbf{W}}_m$ are the weighting matrices for the data and the elements of the material property tensor (which we will call in this section the model parameters). The minimization problem (A1) can be solved using the regularized conjugate gradient (RCG) method (Zhdanov 1993, 2002).

The algorithm of the RCG method can be summarized as follows:

$$\mathbf{r}_n = \widehat{\mathbf{G}}\mathbf{m}_n - \mathbf{d}\,, \qquad (a)$$

$$\mathbf{l}_n^{\alpha_n} = \mathbf{l}^{\alpha_n}(\mathbf{m}_n) = \widehat{\mathbf{G}}^* \widehat{\mathbf{W}}_d^2 \mathbf{r}_n + \alpha_n \widehat{\mathbf{W}}_m^2 (\mathbf{m}_n - \mathbf{m}_{\rm apr})\,, \qquad (b)$$

$$\beta_n^{\alpha_n} = \left\|\mathbf{l}_n^{\alpha_n}\right\|^2 / \left\|\mathbf{l}_{n-1}^{\alpha_{n-1}}\right\|^2, \quad \tilde{\mathbf{l}}_n^{\alpha_n} = \mathbf{l}_n^{\alpha_n} + \beta_n^{\alpha_n} \tilde{\mathbf{l}}_{n-1}^{\alpha_{n-1}}, \tilde{\mathbf{l}}_0^{\alpha_0} = \mathbf{l}_0^{\alpha_0}\,, (c)\,, \tag{A4}$$

$$\tilde{k}_n^{\alpha_n} = \left(\tilde{\mathbf{l}}_n^{\alpha_n *} \mathbf{l}_n^{\alpha_n}\right) / \left[\tilde{\mathbf{l}}_n^{\alpha_n T} \left(\widehat{\mathbf{G}}^* \widehat{\mathbf{W}}_d^2 \widehat{\mathbf{G}} + \alpha \widehat{\mathbf{W}}_m^2 \right) \tilde{\mathbf{l}}_n^{\alpha_n} \right], \qquad (d)$$

$$\mathbf{m}_{n+1} = \mathbf{m}_n - \tilde{k}_n^{\alpha_n} \tilde{\mathbf{l}}_n^{\alpha_n}\,, \qquad (e)$$

where $\mathbf{r}_n$, $\mathbf{m}_n$, α_n, $\mathbf{l}_n^{\alpha_n}$, $\tilde{\mathbf{l}}_n^{\alpha_n}$, $\tilde{k}_n^{\alpha_n}$ and $\beta_n^{\alpha_n}$ are, respectively, the vector of residuals, the vector of model parameters, the regularization parameter, the steepest ascent direction, the conjugate direction, the step length and the conjugate coefficient at the nth iteration. The iterative process (A4) is terminated when the misfit reaches the desired level ε_0 (usually the level of noise in the data):

$$\phi(\mathbf{m}_N) = \|\mathbf{r}_N\|^2 \le \varepsilon_0\,. \tag{A5}$$

The regularization parameter α describes the trade-off between the best fitting and a reasonable stabilization. The basic principles used for determining the regularization parameter α are discussed by Tikhonov & Arsenin (1977) and Zhdanov & Keller (1994). It can be selected from the progression of numbers

$$\alpha_k = \alpha_0 q^k;\ k = 0, 1, 2, \ldots, n;\ 0 < q < 1\,. \tag{A6}$$

For any number α_k we can find an element $\mathbf{m}_{\alpha_k}$, minimizing $P^{\alpha_k}(\mathbf{m})$, and calculate the misfit $\|\widehat{\mathbf{G}}\,\mathbf{m}_{\alpha_k}-\mathbf{d}\|^2$. The optimal value of the parameter α is the number α_{k0}, for which we have

$$\|\widehat{\mathbf{G}}\,\mathbf{m}_{\alpha_{k0}}-\mathbf{d}\|^2=\delta\,, \tag{A7}$$

where δ is the level of noise in the observed data. The equality (A7) is called *the misfit condition*.

In our code we use the *adaptive* RCG method:

$$\tilde{\mathbf{l}}^{\alpha_{n+1}}(\mathbf{m}_{n+1})=\mathbf{l}^{\alpha_{n+1}}(\mathbf{m}_{n+1})+\beta_{n+1}\tilde{\mathbf{l}}^{\alpha_n}(\mathbf{m}_n)\,, \tag{A8}$$

where α_n are the subsequent values of the regularization parameter. In order to avoid divergence, we begin an iteration from a value of α_0, which can be obtained as the ratio of the misfit functional and stabilizer for an initial model, and then reduce α_n according to eq. (A6) on each subsequent iteration and continuously iterate until the misfit condition (A7) is reached.

The matrix of the reflectivity tensor $\boldsymbol{\lambda}_n$ is determined from the matrix $\boldsymbol{m}_n$ using eq. (34):

$$\boldsymbol{\lambda}_n=\mathbf{G}^E\mathbf{m}_n\,. \tag{A9}$$

The anomalous conductivity, $\Delta\tilde{\sigma}_n$, on the nth iteration can be found from eq. (32) using the least-squares method (Zhdanov & Fang 1996b).

Using a minimum norm stabilizer in the expression for the parametric functional results in a smooth inversion result. Imaging sharp geoelectrical boundaries, whenever this is desirable, is made possible using a minimum support functional, which results in a focused inversion model. The method is described by Portniaguine & Zhdanov (1999). We have used this method to produce sharp images with our LQL inversion. Focusing is implemented through the variable weighting matrix $\widehat{\mathbf{W}}_m$ in the RCG method (Zhdanov & Hursan 2000; Zhdanov 2002).

The focusing technique requires setting of upper and lower bounds for the inverted parameter. In our implementation the determination of the upper and lower bounds for the inverted parameter is slightly different from that of Portniaguine & Zhdanov (1999). They assume that the upper and lower bounds of the anomalous conductivity are known approximately. In our case, since we are not inverting for the anomalous conductivity $\Delta\sigma$, but for the modified material property tensor $\widehat{\boldsymbol{m}}$, the definition of these bounds is slightly more complicated. Specifically, we determine these bounds using the relation $\widehat{\boldsymbol{m}}=\Delta\sigma\ (\hat{\boldsymbol{I}}+\hat{\boldsymbol{\lambda}})$. Assuming that we know the upper and lower bounds of $\Delta\sigma$ approximately, we have tabulated the approximate values of $\hat{\boldsymbol{\lambda}}$ within the anomalous domain, by performing a simple modelling study. This is done by calculating the anomalous and background electric fields inside the anomalous domain and using the relation $E^{\mathrm{a}}=\hat{\boldsymbol{\lambda}}E^{\mathrm{b}}$. It has been shown (Zhdanov & Fang 1996a) that the value of $\boldsymbol{\lambda}$ inside the anomalous domain varies very slowly, and it does not vary greatly with frequency either. It is therefore sufficient to calculate $\boldsymbol{\lambda}$ only for a few models. Then, knowing (approximately) the bounds of $\Delta\sigma$ and $\hat{\boldsymbol{\lambda}}$, we find the corresponding bounds for $\widehat{\boldsymbol{m}}$ from the relation $\widehat{\boldsymbol{m}}=\Delta\sigma(\hat{\boldsymbol{I}}+\hat{\boldsymbol{\lambda}})$.